

# Measurement of the position resolution of the Gas Pixel Detector

Paolo Soffitta<sup>1</sup>, Fabio Muleri, Sergio Fabiani, Enrico Costa

*IAPS/INAF Via Fosso del Cavaliere 100, 00133-Roma, Italy*

Ronaldo Bellazzini, Alessandro Brez, Massimo Minuti,  
Michele Pinchera, Gloria Spandre

*INFN-Pisa Largo B. Pontecorvo, 3 - 56127 Pisa, Italy*

---

## Abstract

The Gas Pixel Detector was designed and built as a focal plane instrument for X-ray polarimetry of celestial sources, the last unexplored subtopics of X-ray astronomy. It promises to perform detailed and sensitive measurements resolving extended sources and detecting polarization in faint sources in crowded fields at the focus of telescopes of good angular resolution. Its polarimetric and spectral capability were already studied in earlier works. Here we investigate for the first time, with both laboratory measurements and Monte Carlo simulations, its imaging properties to confirm its unique capability to carry out imaging spectral-polarimetry in future X-ray missions.

*Keywords:*

X-ray; astronomy; detectors; polarimetry

---

## 1. Introduction

The Gas Pixel Detector (GPD) [1, 2, 3] has been designed and built to perform time resolved imaging spectral-polarimetry of X-ray celestial sources by means of the photoelectric effect. It is the long sought quantum leap in sensitivity with respect to the classical techniques [4]. Successively the same

---

*Email address:* [paolo.soffitta@iaps.inaf.it](mailto:paolo.soffitta@iaps.inaf.it) ()

<sup>1</sup>Corresponding Author

method was implemented exploiting an alternative technique without any 2-D imaging capability [11].

While the polarimetric and the spectroscopic performances of the GPD have been already studied in detail [5, 6], its imaging properties have been estimated, so far, only by Monte Carlo simulations evaluating the point of conversion of the impinging photon with a suitable algorithm [9]. Still the GPD was devised primarily to be exploited at the focus of conventional and multi-layer hard X-ray optics [22]. At this purpose the GPD has been considered for different proposed space missions [14, 12, 13, 15]. While X-ray optics with the exquisite quality of those of Chandra will not be again available in the near future, for POLARIX (or XIPE, proposed in 2012 to ESA as a small mission for a launch on 2017) the JET-X optics (three complete mirrors, two Flight Models, FM, the heritage of the former Spectrum X-Gamma mission, and one Qualification Model), can still be used. They have a Point Spread Function (PSF) with a measured Half Energy Width (HEW) at 1.5-keV of 15.1" (FM-1) and 14.6" (FM-2) [7].

We report on the first measurement, with a narrow beam at 4.5 keV, of the position resolution of a GPD filled with a mixture of He-DME 80-20 (1 bar) with a large Gas Electron Multiplier (GEM). This proves the capability of the GPD to perform space-resolved measurements, such as those of Pulsar-Wind Nebulae, Supernova Remnants or X-ray jets with a suitable accuracy, and to observe the faintest source accessible to X-ray polarimetry especially in crowded fields [20]. We also compared such measurement with the Monte Carlo simulation relating the characteristics of the image to the modulation factor. Finally we showed the effect on imaging of the non-uniformity of the drift electric field in case the GEM plane, and in particular the guard-ring, is not powered.

## 2. The GPD prototype and the relevant algorithms

The GPD is a gas cell with a beryllium thin window, a drift region, a perforated multiplication plane (the GEM) and a collecting plane with an hexagonal pattern.

The collecting (or readout) plane is the top layer of an ASIC CMOS with a square surface of 1.5 cm  $\times$  1.5 cm having 105600 hexagonal pads of 50  $\mu$ m pitch. It is designed with a very high precision due to the micro-electronics technologies employed. The positions of the hexagonal pads set

up, therefore, a very high accurate reference system which is essential for an accurate imaging.

Hereafter we summarize, to understand the considerations in the following sections, the sequential steps of the algorithm that processes the signal from each hexagonal pad that collects the charges of the track. The algorithm is aimed to evaluate:

- the *barycentre* using all the pixels;
- the *angle*, for which the second moment, with respect to the barycentre, is maximum;
- the *third moment* (skewness), also with respect to the barycentre, to determine which of the two end points contains the impact point (by the smaller charge density);
- the *impact point*, using the pixel only within a sub-region of the initial part of the track as it is identified by the skewness. The extension of this sub-region depends on the gas mixture and it is evaluated by using the maximum second moment as a weight;
- the *angle* (emission direction) that maximizes the second moment with respect to the impact point weighting the charges according to their distance from it.

The first sealed GPD [3] had a GEM plane with the perforated surface as large as the ASIC CMOS chip and a guard-ring, not perforated, just slightly larger. The present prototype [19] has, instead, a much larger guard-ring extending as far as 2.25 cm from the edge of the ASIC chip. This latter design, see fig. 1(a) and fig. 1(b) for a comparison, allows for a better control of the uniformity of the electric field. Border effects, other than those due to the extension of the track and to its incomplete imaging close to the edge of the sensitive region, are now therefore expected to be vanishing. We will show later how the guard-ring influences the position resolution of the GPD.

The GPD has a drift/absorption length of 1 cm and a beryllium window 50  $\mu\text{m}$  thick. The GEM employed with this new design is 50  $\mu\text{m}$  thick, with holes of 30  $\mu\text{m}$  of diameter with 50  $\mu\text{m}$  pitch. The holes are laser etched on a liquid crystal polymer substrate. The GEM is manufactured by SciEnergy under the supervision of RIKEN [16].

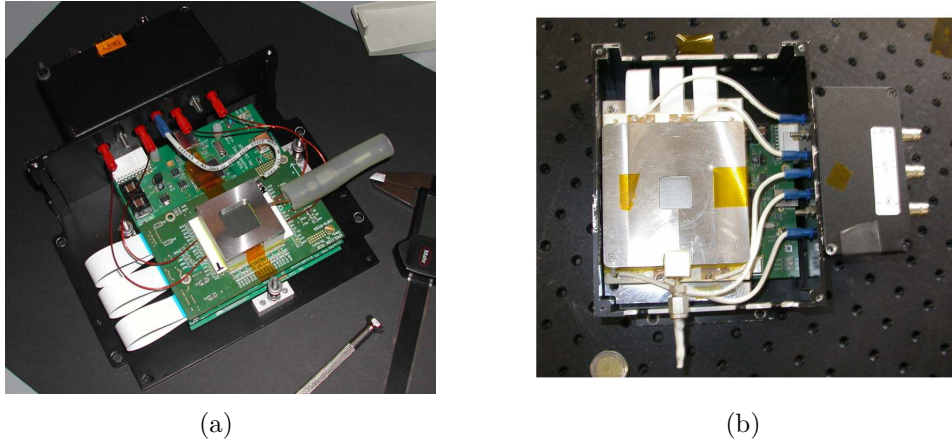


Figure 1: (a). The old design of the GPD with a narrow guard-ring in the GEM plane (b). The present design with a larger guard-ring [19].

### 3. The X-ray beam profile

In order to measure the position resolution we arranged a narrow X-ray beam by means of a collimator system connected to the exit beryllium window of a 50 W (50 kV, 1 mA) commercial X-ray tube with a Titanium anode by Oxford Instruments (series 5000) having an anode spot smaller than  $150 \mu\text{m}$ . The X-rays from the tube, operated at 30 kV and  $400 \mu\text{A}$ , were collimated by means of two diaphragms, one made of brass having a diameter of  $500 \mu\text{m}$  connected to the exit window of the X-ray tube and one made of tungsten with a diameter of  $25 \mu\text{m}$  on the opposite side close to the detector window. The two diaphragms were interconnected by two coaxial brass shielding tubes and separated by 17 cm. The large distance necessary to reduce the beam divergency does not allow for measuring the position resolution at energies below the Titanium X-ray K lines at 4.51 keV ( $K_\alpha$ ) due to the intervening air absorption. In order to measure the actual beam size, we scanned the X-ray beam with a brass slit with sharp edges, at the same distance of the GPD, in two orthogonal directions and at a constant speed using as detector a commercial one-pixel Si-PIN XR-100-CR manufactured by Amptek. The geometrical surface of the detector is  $5 \text{ mm} \times 5 \text{ mm}$ . This system, when interfaced to the two orthogonal linear stages with  $0.5 \mu\text{m}$  resolution (model ILS50CC), manufactured by Newport and operated via computer by means of an 8-axis XPS controller [21], allows for continuously shifting the detector and the slit with respect to the beam at a

minimum speed of  $1 \mu\text{m s}^{-1}$ . Data from the Si-PIN detector were acquired in rate-meter mode with a time-bin of 1 s, selecting a window in energy to include only the titanium K-lines. With this set-up, the time needed for obscuring the beam at the slit passage provides the beam size along the direction of the scan.

If the beam is described by a 2-D gaussian, as in the following equation 1) :

$$f(X, Y) = Ae^{-\left(\frac{(X-X_0)^2}{2\sigma_X^2} + \frac{(Y-Y_0)^2}{2\sigma_Y^2}\right)} \quad (1)$$

the counting rate as a function of time (or as a function of position being the speed constant and known) resulting from the scanning along the X (or Y) direction can be described by the *erf* function as in eq. 2. This is, actually, the primitive of eq. 1 after the integration between  $-\infty$  and  $+\infty$  of the counts in Y (or X) direction.

The counting rate during the scanning in Y and X are shown in figure 2 together with the fitting function :

$$f(X) = \frac{A_X}{2} \left[ 1 - \operatorname{erf}\left(\frac{\sqrt{2}(X - X_0)}{2\sigma_X}\right) \right] \quad (2)$$

Such fitting procedure allows for deriving the relevant parameters ( $\sigma_X$  and  $\sigma_Y$ ) of the X-ray beam and comparing them with the results of the section 4. The results of the fit are shown in the table 1:

Table 1: Result of fitting procedure of the beam scan. The  $\chi^2_\nu$  is 1.0 for the X scan and 1.12 for Y scan.

Param	Fit results
$A_X$	$(171.71 \pm 1.21)$ Counts/s
$X_0$	$(132.42 \pm 0.31)$ $\mu\text{m}$
$\sigma_X$	$(8.7 \pm 0.3)$ $\mu\text{m}$
$A_Y$	$(171.67 \pm 1.16)$ Counts/s
$Y_0$	$(152.41 \pm 0.78)$ $\mu\text{m}$
$\sigma_Y$	$(14.7 \pm 0.4)$ $\mu\text{m}$

The beam shape is therefore consistent with being gaussian with two different elongation in the two orthogonal directions. Such different elongations

may be due either to the position of the  $500 \mu\text{m}$  diaphragm with respect to the anode spot of the X-ray tube or to a possible residual misalignment between the two small diaphragms at the opposite end of the two collimator brass tubes.

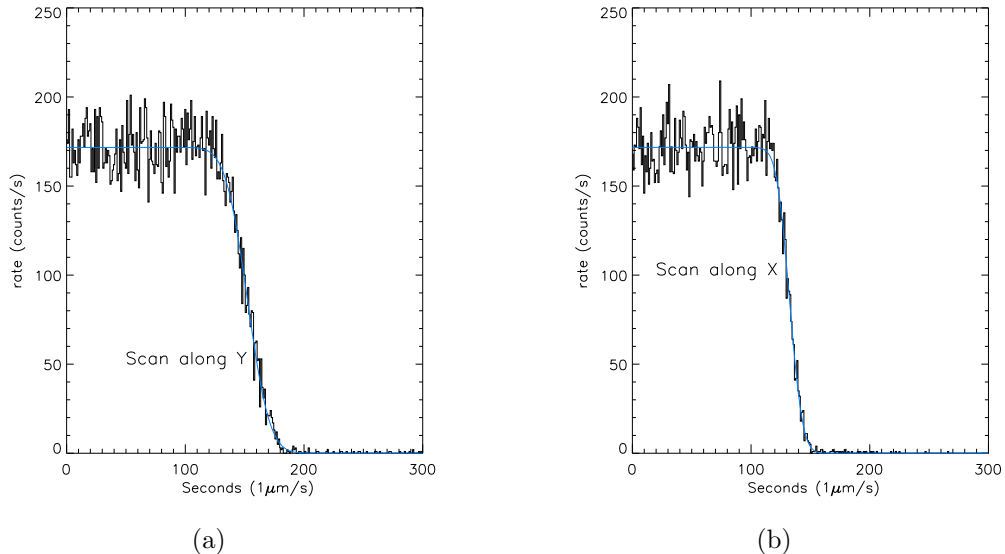


Figure 2: (a). Scan along the Y axis. The result from fitting eq 2 is  $\sigma_Y = (14.7 \pm 0.4) \mu\text{m}$  (b). Scan along the X axis. The result from fitting eq 2 is  $\sigma_X = (8.7 \pm 0.3) \mu\text{m}$ .

We did not investigate further the cause of the two different sizes since their values are already smaller than the expected position resolution of the GPD.

#### 4. The position resolution determination

To study the imaging capability of the GPD we made a set of three measurements shifting it by  $300 \mu\text{m}$  with respect to the central position (the center of the ASIC chip readout plane) in orthogonal directions. This central position was, actually, found manually by iterating once the shift and the derived centroid of the image of the beam.

The counting rate during each acquisitions was about  $10 \text{ counts } s^{-1}$ , by far larger than the background counting rate, for a total of about 8700 counts/acq., all windowed in energy to include only the Ti  $K$  photo-peak. The images of the three acquisitions all together are displayed in figure 3

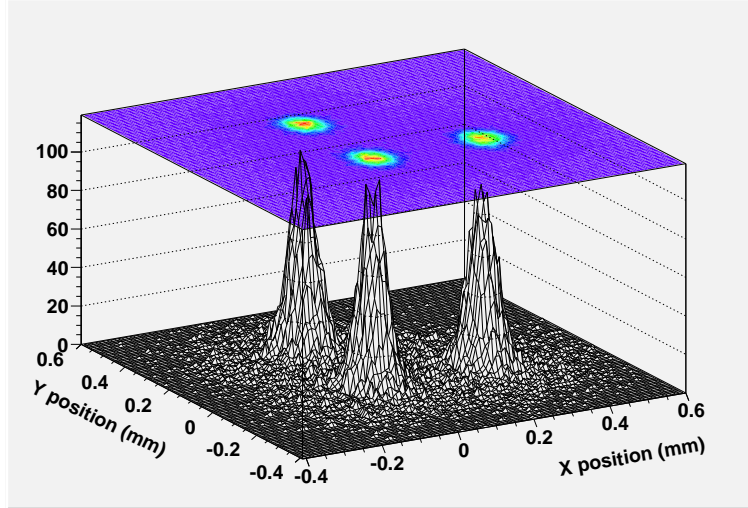


Figure 3: The real images of the beam detected by the GPD. These images were obtained by shifting the GPD by  $300 \mu\text{m}$  in orthogonal directions with respect to the central position.

where they appear well separated. A closer view shows that they are characterized by a dominating core with external wings. We investigated the properties of the core and the wings in detail later in section 5 by means of Monte Carlo simulations. In this section we, instead, measured the properties of the core. A bi-dimensional gaussian including two free  $\sigma_X$  and  $\sigma_Y$  parameters (see eq.1) was fitted to the data considering only the central part of the impact point distribution in a frame of  $120 \mu\text{m} \times 170 \mu\text{m}$  around the peak position. The fit was performed by using the MINUIT package included in the ROOT 5.0 environment. The results of the fit are shown in the table 2. The  $\chi^2$  of the fit of the core was 200.9 with 196 degree of freedom. A close-up view of the image of beam in the central position and the fitted function are shown in figure 4(a) and 4(b).

Having determined in section 3 the main parameters of the beam profile we are in the position to correct the measured values. We subtracted quadratically the size of the beam as derived in table 1 from the position resolution of the GPD as in table 2. The results for the two standard deviations are  $\sigma_X^{GPD} = (28.1 \pm 0.5) \mu\text{m}$  and  $\sigma_Y^{GPD} = (34.3 \pm 0.6) \mu\text{m}$ . The remaining significative, albeit small, difference in size between the two directions could be due to the different sampling in X and Y because of the hexagonal readout pattern. While X is sampled with  $50 \mu\text{m}$  resolution, thus the hexagonal pitch,

Table 2: Fit results of the real data acquired by the GPD in the central position, in a frame of  $120 \mu\text{m} \times 170 \mu\text{m}$  around the peak position, using the 2-D gaussian of equation 1.

Param.	Fit results
$A$	$95.36 \pm 1.91$ counts
$X_o$	$(2.1 \pm 0.4) \mu\text{m}$
$Y_o$	$(-17.4 \pm 0.5) \mu\text{m}$
$\sigma_X$	$(29.5 \pm 0.4) \mu\text{m}$
$\sigma_Y$	$(37.3 \pm 0.4) \mu\text{m}$

$Y$  is sampled with a resolution of  $50 \mu\text{m} \times \cos(30^\circ) = 43.3 \mu\text{m}$ . However we cannot exclude, also, a residual misalignment of the X-ray beam axis with respect to the GPD plane and the effect on the different elongation due to the inclined penetration. The control of such angle is, indeed, mostly relied on machined parts and an alignment procedure based on measurements at controlled different inclinations will be studied. For the time-being we retain that  $\sigma_X^{GPD}$  and  $\sigma_Y^{GPD}$  are close enough to assess that no major problems in the set-up, in the CMOS ASIC read-out or in the algorithm are present.

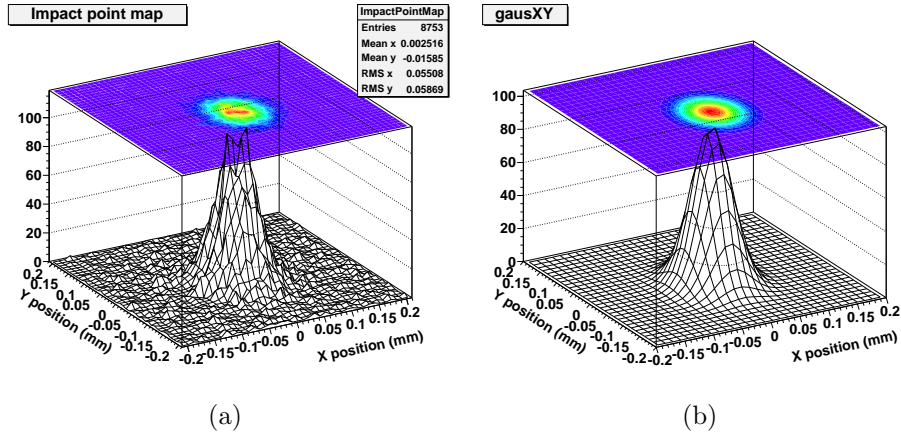


Figure 4: (a). A close-up of the image of the central beam. (b). 2-D Gaussian function fitted to the core of the image.

## 5. The Monte Carlo simulation of the beam profile

A simulation was performed with the Monte Carlo we routinely use to anticipate the polarimetric performances of the GPD. The Monte Carlo simulates the generation, the transport, the multiplication and the collection of the Auger-electrons tracks and of the photoelectron tracks from different atom shells. Such tracks are generated by X-rays of a given polarization degree and of a given energy in a given gas mixtures. The main routines of the Monte Carlo were earlier described in [23, 9, 10]. The simulated data are processed by algorithms equivalent to those used for the real data collected by the GPD. The agreement between the Monte Carlo and the experimental data in terms of modulation factor was already studied for different gas mixtures and detectors, see [5, 6, 19]. Here, instead, we compare the position resolution. At this regards we simulated a narrow pencil beam of 4.5 keV unpolarized photons impinging on the center of the GPD. For each simulated track we derived the reconstructed impact point, together with the reconstructed emission direction. The total number of counts in the simulation is larger with respect to the acquired real data of a factor of about 3. The location of the impact points resulting from the simulation is shown in figure 5. The presence of a core and external wings, evident in this image, will be characterized in section 5.1 and 5.2. In this paragraph we show the results of the fitting procedure to determine the parameters of the simulated image profile.

Such image profile, together with the 2-D gaussian function used to fit the data (within a square wide  $110 \mu\text{m} \times 110 \mu\text{m}$ ), is, indeed, displayed in figure 6(a) and 6(b) respectively.

Table 3: Results of the fitting of the core of the simulated beam image with the 2-D gaussian function of equation 1.

Param.	Fit results
$A$	$363.9 \pm 4.4$ counts
$x_o$	$(0.00 \pm 0.02) \mu\text{m}$
$y_o$	$(0.00 \pm 0.08) \mu\text{m}$
$\sigma_x$	$(30.8 \pm 0.3) \mu\text{m}$
$\sigma_y$	$(31.9 \pm 0.3) \mu\text{m}$

The results of the fit are in table 3 and the  $\chi^2_\nu$  is now 2.2. Such a large

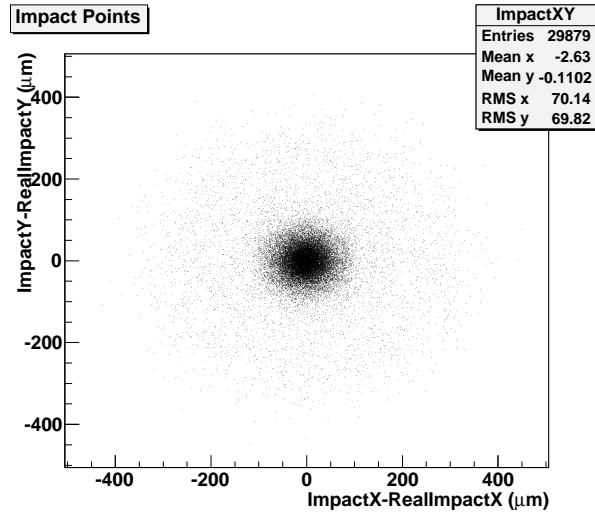


Figure 5: Scatter plot of the reconstructed impact points from simulated data. Wings are defined as the set of impact points outside a core of  $200 \mu\text{m}$  of diameter.

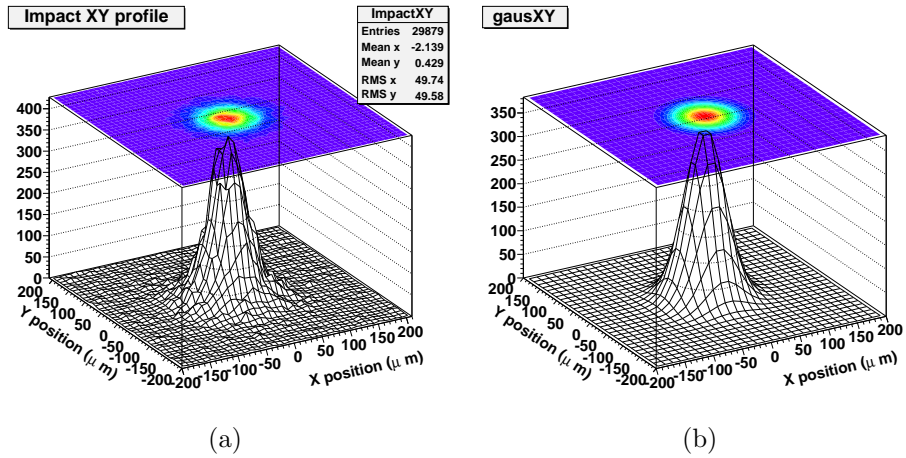


Figure 6: (a). Monte Carlo simulation of a narrow beam of  $4.5 \text{ keV}$  as imaged by the GPD. (b). Gaussian fit of the core (within a square wide  $110 \mu\text{m} \times 110 \mu\text{m}$ ) of the simulated data.

value may be is due to the contribution of the wings which are included in the corner of the selected region. Actually fitting the same function on a larger set of the data (a square wide of  $130 \mu\text{m} \times 130 \mu\text{m}$ ), the  $\chi^2_\nu$  increases to 2.5 probably because of the larger contribution of the wings.

If we compare the results of table 3 with  $\sigma_X^{GPD}$  and  $\sigma_Y^{GPD}$ , we see that they agree within about  $3 \mu\text{m}$ . The agreement is very good also considering that the simulated beam is aligned by construction with respect to the GPD plane.

### 5.1. The core and wings in the simulated image

Puzzled by the presence of the wings, we used the Monte Carlo data to investigate their origin and to study their contribution to the sensitivity for polarimetry. With the Monte Carlo is, indeed, easier to relate the evolution of the original simulated track to the event detected by the GPD after transport, blurring, multiplication and collection. The exact definition of the core and the wings is beyond the scope of this paper. Therefore we define, somewhat arbitrarily, the core as the region inside  $200 \mu\text{m}$  in diameter from the peak position, and the wings as the set of the impact points outside the core. With this definition in mind we compared the detected number of events with those expected by the 2-D symmetrical gaussian function. We recall that the density of probability (equation 1) with the normalization constant  $\frac{1}{2\pi \times \sigma^2}$ , if circularly symmetric, can be written as :

$$f(r) = \frac{1}{\sigma^2} \times r \times e^{-\frac{r^2}{2\sigma^2}} \quad (3)$$

The fraction of events outside a circle of radius  $r_0$  can be written as in equation 4 :

$$\int_{r_0}^{\infty} f(r) dr = e^{-\frac{r_0^2}{2\sigma^2}} \quad (4)$$

The fraction of the reconstructed impact points outside a radius of  $100 \mu\text{m}$  in the Monte Carlo data is indeed 16.6 %, while the expected fraction is only 0.5 %. This excess represents the contribution of the wings. The investigation of the wings is important because some wings are, generally, present also in the Lorentian PSF of the X-ray optics [17, 18] and an interplay between the two could be expected in focal plane experiments.

An inspection of the Monte Carlo tracks with calculated positions outside the core showed that the presence of wings is due, indeed, to an incorrect determination of the reconstructed impact point. In practice the reconstructed impact point is on the opposite side with respect to real impact point. This happens because the algorithm calculates the skewness for determining the end point of the track (see section 2) containing the Bragg peak that is the end of the photoelectron evolution. The distribution of charges for some kind of trajectories provides blurred collected tracks with the skewness giving the 'wrong' sign. Consequently, instead to identify in the track the correct end point, the incorrect one is derived. A simulated track where this inversion happens is shown in figure 7(a) where it is displayed its projection on the X & Y plane (the GPD readout plane) in the Monte Carlo coordinate system. In figure 7(b) it is shown the image of the same track blurred by diffusion, multiplied by the GEM and collected by the readout plane. The green cross, in the latter, is the original impact point, the blue cross is the barycentre and, finally, the red cross is the reconstructed position. An inspection of the original track shows, see figure 7(a), that the impact point in the original frame coordinates is at ( $X = 0$ ;  $Y = 0$ ), the Auger-electron evolves rightwards while the photoelectron firstly evolves in the same semi-plane containing the Auger-electron, secondly scatters on a nuclei and moves on the opposite semi-plane. The derived distribution of the blurred charge is such that a larger density is at the end point containing the original impact point and not at the opposite end point containing the Bragg peak: the evaluation of the skewness, therefore, produces an inversion. A consequence of such an error is that the emission direction is, also, changed (see again figure 7(b) and its caption) and almost inverted. Due to the  $180^\circ$  symmetry a certain, albeit smaller, sensitivity to polarization is expected to be preserved also in the events contained in the wings. This is the object of the study presented in the section 5.2.

### *5.2. The core and wings: the impact on the polarization sensitivity*

We studied also by Monte Carlo simulations the contribution of the core and wings to the polarimetric sensitivity of the GPD. Such study, in our laboratory, at the present time can only be done by simulation. The generation of polarized radiation, in our facility, greatly reduces the flux from the X-ray tube and, therefore, the use of a collimator system with a narrow beam in addition to the polarizer is of no practical use.

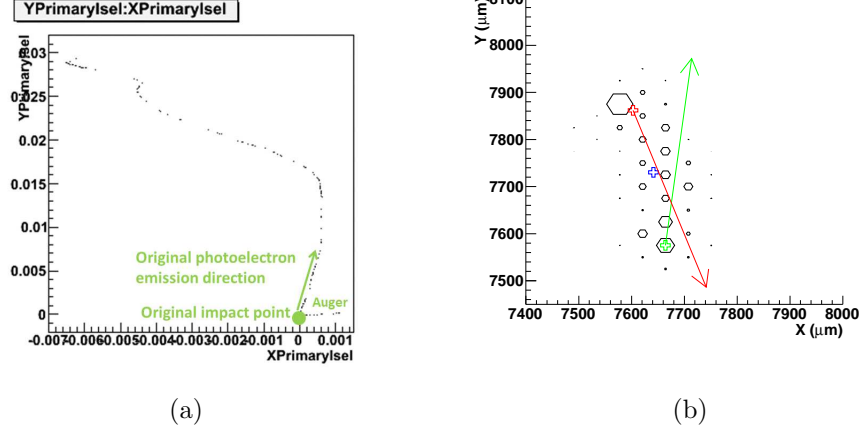


Figure 7: (a). A simulated track in the wings projected on the GPD plane. (b). The same simulated track after transport, blurring, multiplication and collection. The green cross and the arrow line is the original impact point with the emission direction while the red cross and arrow line is the reconstructed impact point and the reconstructed emission direction.

However the agreement between the Monte Carlo data and the experimental data, both in terms of modulation factor and position resolution, is such that a comparative study of the wings and the core in terms of polarization sensitivity is reasonable in this way.

We simulated for this study a zero-width narrow X-ray beam of 4.5 keV and 100 % polarized and we derived the reconstructed impact point and the emission direction for each event. The histogram of the emission directions, the so called modulation curve, is reported in figure 8(a) and in figure 8(b) for the core and the wings respectively with the following function to derive the modulation factor :

$$f(\phi) = A + B\cos^2(\phi - \phi_0) \quad (5)$$

where A and B and  $\phi_0$  are parameters of the fit. The modulation factor  $\mu$  is given by the equation 6 :

$$\mu = \frac{B}{2A + B} \quad (6)$$

The modulation factor of the whole data set is  $\mu = (50.9 \pm 0.6) \%$ . The contribution of the core is  $\mu = (55.3 \pm 0.6) \%$  and the contribution of the

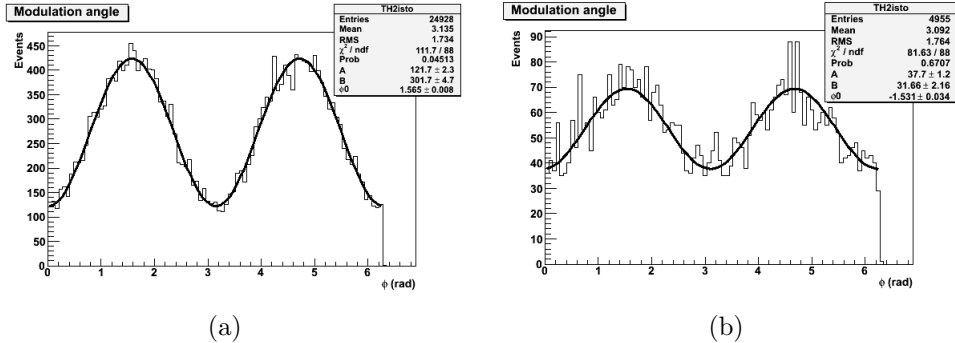


Figure 8: (a). Modulation curve from simulated 100% polarized 4.5-keV photons in the core. The modulation factor is  $\mu = (55.3 \pm 0.6) \%$ . (b). Modulation curve from simulated 100% polarized 4.5-keV photons in the wings. The modulation factor is  $\mu = (29.6 \pm 1.6) \%$ .

wings decreases down to  $\mu = (29.6 \pm 1.6) \%$ . We therefore demonstrated that the core, as expected, has a larger polarization sensitivity with respect to the wings. This is interesting because, by selecting the events contained in the core, we could determine the polarization of a point-like celestial source with a better confidence. We recall, actually, that the polarization sensitivity is proportional to the so called quality factor (equation 7) :

$$QF = \mu\sqrt{\varepsilon} \quad (7)$$

where  $\varepsilon$  is the efficiency. In our case  $QF_{core} = 0.505$  and  $QF_{all} = 0.509$  therefore basically identical, however the larger modulation factor obtainable selecting only the events in the core allows for a slightly better control of the incidence on the measurement of possible residual systematics. Moreover the lower, but not zero, modulation factor of the wings allow for using these events once properly weighted. In any case the analysis shows that the main origin of the wings is that, for a fraction of events, mainly those characterized by photoelectrons that underwent to a large scattering angle with an atomic nucleus, the skewness is not sufficient to identify the section of the track that includes the impact point. This means that an improved pattern recognition can be mitigates significantly the problem.

The effects on sensitivity of the selection of the core and the wings needs a more accurate study. For example they are expected to be energy dependent through the different average size and shape of the tracks. Such study is beyond the scope of this work, but we recall that spectral capability of the

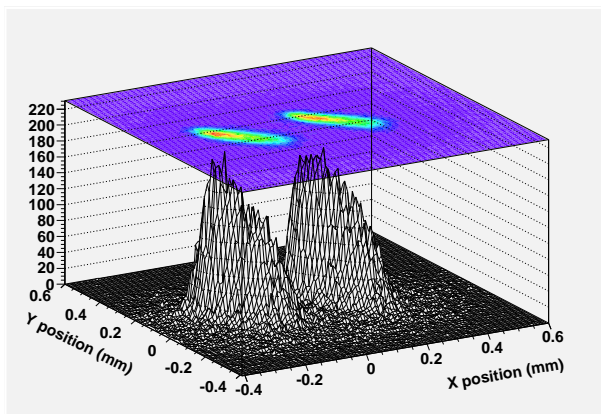


Figure 9: Distortion of the two images of the beam shifted  $300\ \mu\text{m}$  after the disconnection of the upper guard-ring.

GPD allows for such an investigation.

## 6. The effect of the large guard-ring on the image profile

The two different configurations up to now used for the GPD, the old configuration, with a small guard-ring in the GEM plane, and the present configuration, with a larger guard-ring, were already described in section 2. We can not directly compare the two configurations in terms of position resolution, since the old configuration is not available at the moment, but we can show the effect of the presence of the guard-ring on the location capability of the detector. Therefore, to study how the uniformity of the electric field impacts on the image of the narrow beam, we disconnected the upper guard-ring of the GEM plane. The results are shown in fig. 9 for two of the three positions of fig. 3. The effect is indeed enormous. The image of the beam appear now larger, distorted and rotated even at the center of the active region at about  $7.5\ \text{mm}$  from its border.

The electric-field, with this disconnection, is not the same of that of the old-one, with a smaller guard-ring and a smaller aspect ratio (the ratio between the thickness of the drift region and the linear dimension of the surface area of the GEM plane). However this measurement suggests that the present configuration assures better performances in terms of drift-field uniformity and position resolution capability.

## 7. Conclusions

We studied the position resolution of the GPD by means of laboratory measurements and Monte Carlo simulations, at 4.5 keV, using a narrow X-ray beam. After subtracting the contribution of the beam size which was measured by means of a scanning technique, we obtained a position resolution more than twice better than that already found with a Micro Pattern Gas Detector with 200  $\mu\text{m}$  pitch and a GEM with a larger pitch [9]. The measured position resolution is very close to the Monte Carlo results. By using the latter and equation 4, the Half Energy Width (HEW, spatial) found is 36.3  $\mu\text{m}$ . The expected HEW (spatial) by the JET-X optics (with a focal length of 3500 mm and a HEW (angular) of 19.3" [8]), is 327  $\mu\text{m}$ , a factor of nine larger, including also the effects of inclined penetration of the photons collected in the absorption depth of the GPD. The angular resolution of an experiment with the GPD at the focus of such X-ray optics is, therefore, driven primarily by the quality of the latter.

We detected the presence of wings in the image of the beam in both the real data and the Monte Carlo data. Such wings were studied primarily by simulations and are due to an inversion in the location of the impact point due to peculiar event trajectories and to the blurring. The core events have a larger modulation factor with respect to the events in the wings suggesting that a spatial selection of the data, a different weight, or a better pattern recognition, especially for polarimetry of point-like celestial sources, would lead to an improved statistical significance.

Finally we showed the effect of the presence of the large guard-ring on the image profile of the narrow beam.

## 8. Acknowledgment

This work is partially supported by the Italian Space Agency (ASI).

## References

- [1] Costa, E., Soffitta, P., Bellazzini, R., et al., *Nature* 411 (2001) 662
- [2] Bellazzini, R., Spandre, G., Minuti, M., et al., *Nuclear Instruments and Methods in Physics Research Section A* 566 (2006) 552
- [3] Bellazzini, R., Spandre, G., Minuti, M., et al., *Nuclear Instruments and Methods in Physics Research Section A* 579 (2007) 853

- [4] Soffitta, P., Baldini, L., Bellazzini, R., et al., Nuclear Instruments and Methods in Physics Research Section A 510 (2003) 170
- [5] Muleri, F., Soffitta, P., Baldini, L., et al., Nuclear Instruments and Methods in Physics Research Section A 584 (2008) 149
- [6] Muleri, F., Soffitta, P., Baldini, L., et al., Nuclear Instruments and Methods in Physics Research Section A 620 (2010) 285
- [7] Wells, A. A., Castelli, C. M., Denby, M., et al., Proc. SPIE 3114 (1997) 392
- [8] Lazzarotto, F., & et al. 2010, X-ray Polarimetry: A New Window in Astrophysics by Ronaldo Bellazzini, Enrico Costa, Giorgio Matt and Gianpiero Tagliaferri (Eds.) Cambridge University Press, 2010., p. 79
- [9] Bellazzini, R., Angelini, F., Baldini, L., et al., Proc. SPIE 4843 (2003) 383
- [10] Pacciani, L., Costa, E., Di Persio, G., et al. Proc. SPIE, 4843 (2003) 394
- [11] Black, J. K., Baker, R. G., Deines-Jones, P., Hill, J. E., & Jahoda, K., Nuclear Instruments and Methods in Physics Research A 581 (2007) 755
- [12] Costa, E., Bellazzini, R., Tagliaferri, G., et al., Experimental Astronomy 28 (2010) 137
- [13] Bellazzini, R., & et al. 2010, X-ray Polarimetry: A New Window in Astrophysics; Ronaldo Bellazzini, Enrico Costa, Giorgio Matt and Gianpiero Tagliaferri (Eds.) Cambridge University Press, 2010., p. 269
- [14] Soffitta, P., Bellazzini, R., Tagliaferri, G., et al., Proc. SPIE 7011 (2008) 62
- [15] Soffitta, P., Costa, E., Muleri, F., et al., Proc. SPIE 7732 (2010) 38
- [16] Tamagawa, T., & et al. 2010, X-ray Polarimetry: A New Window in Astrophysics; Ronaldo Bellazzini, Enrico Costa, Giorgio Matt and Gianpiero Tagliaferri (Eds.) Cambridge University Press, 2010., p. 60,

- [17] Citterio, O., Conconi, P., Ghigo, M., et al., Proc. SPIE 2279 (1994) 480
- [18] Citterio, O., Campano, S., Conconi, P., et al., Proc. SPIE 2805 (1996) 56
- [19] Muleri, F., Bellazzini, R., Brez, A., et al., Proc. SPIE 8443 (2012) in press
- [20] Soffitta, P., Campana, R., Costa, A., et al., Proc. SPIE 8443 (2012) in press
- [21] Muleri, F., Soffitta, P., Bellazzini, R., et al., Proc. SPIE (2008) 7011, 61
- [22] Muleri, F., Bellazzini, R., Costa, E., et al., Proc. SPIE 6266 (2006) 85
- [23] Soffitta, P., Costa, E., di Persio, G., et al., Nuclear Instruments and Methods in Physics Research Section A, 469 (2001) 164